ADVANCED
SCIENCE NEWS
www.advancedsciencenews.com

NANO · MICRO
small

2D Materials

Anisotropic Spectroscopy and Electrical Properties of 2D $ReS_{2(1−x)}Se_{2x}$ Alloys with Distorted 1T Structure

Wen Wen, Yiming Zhu, Xuelu Liu, Hung-Pin Hsu, Zhen Fei, Yanfeng Chen, Xinsheng Wang, Mei Zhang, Kuan-Hung Lin, Fei-Sheng Huang, Yi-Ping Wang, Ying-Sheng Huang, Ching-Hwa Ho, Ping-Heng Tan, Chuanhong Jin, and Liming Xie*

2D black phosphorus (BP) and rhenium dichalcogenides (ReX_2, X = S, Se) possess intrinsic in-plane anisotropic physical properties arising from their low crystal lattice symmetry, which has inspired their novel applications in electronics, photonics, and optoelectronics. Different from BP with poor environmental stability, ReX_2 has low-symmetry distorted 1T structures with excellent stability. In ReX_2, the electronic structure is weakly dependent on layer numbers, which restricts their property tunability and device applications. Here, the properties are tuned, such as optical bandgap, Raman anisotropy, and electrical transport, by alloying 2D ReS_2 and $ReSe_2$. Photoluminescence emission energy of $ReS_{2(1−x)}Se_{2x}$ monolayers (x from 0 to 1 with a step of 0.1) can be continuously tuned ranging from 1.62 to 1.31 eV. Polarization behavior of Raman modes, such as ReS_2-like peak at 212 $cm^{−1}$, shifts as the composition changes. Anisotropic electrical property is maintained in $ReS_{2(1−x)}Se_{2x}$ with high electron mobility along b-axis for all compositions of $ReS_{2(1−x)}Se_{2x}$.

1. Introduction

2D layered semiconductors, such as transition metal dichalcogenides (TMDs) and black phosphorus (BP), are emerging materials for next-generation atomically thin electronic and optoelectronic applications, owing to their atomic thickness, strong light–matter interactions, and mechanical flexibility.[1–5] 2D anisotropic materials, such as BP and rhenium dichalcogenides (ReX_2, X = S, Se), are a special 2D material category which has a low crystal lattice symmetry[6,7] thus giving rise

Dr. W. Wen, Dr. Y. Zhu, Dr. Y. Chen, Dr. X. Wang, Dr. M. Zhang, Prof. L. Xie
CAS Key Laboratory of Standardization and Measurement for Nanotechnology
National Center for Nanoscience and Technology
Beijing 100190, P. R. China
E-mail: xielm@nanoctr.cn

Dr. W. Wen, Dr. M. Zhang, Prof. L. Xie
University of Chinese Academy of Sciences
Beijing 100049, P. R. China

Dr. X. Liu, Prof. P.-H. Tan
State Key Laboratory of Superlattices and Microstructures
Institute of Semiconductors
Chinese Academy of Sciences
Beijing 100083, China

Dr. H.-P. Hsu
Department of Electronic Engineering
Ming Chi University of Technology
Taipei 243, Taiwan, Republic of China

Dr. Z. Fei, Prof. C. Jin
State Key Laboratory of Silicon Materials
School of Materials Science and Engineering
Zhejiang University
Hangzhou 310027, P. R. China

Dr. K.-H. Lin, Dr. F.-S. Huang, Dr. Y.-P. Wang,
Prof. Y.-S. Huang
Department of Electronic Engineering
National Taiwan University of Science and Technology
Taipei 106, Taiwan, Republic of China

Y. Zhu
Department of Applied Physics
Chongqing University
Chongqing 401331, P. R. China

Dr. C.-H. Ho
Graduate Institute of Applied Science and Technology
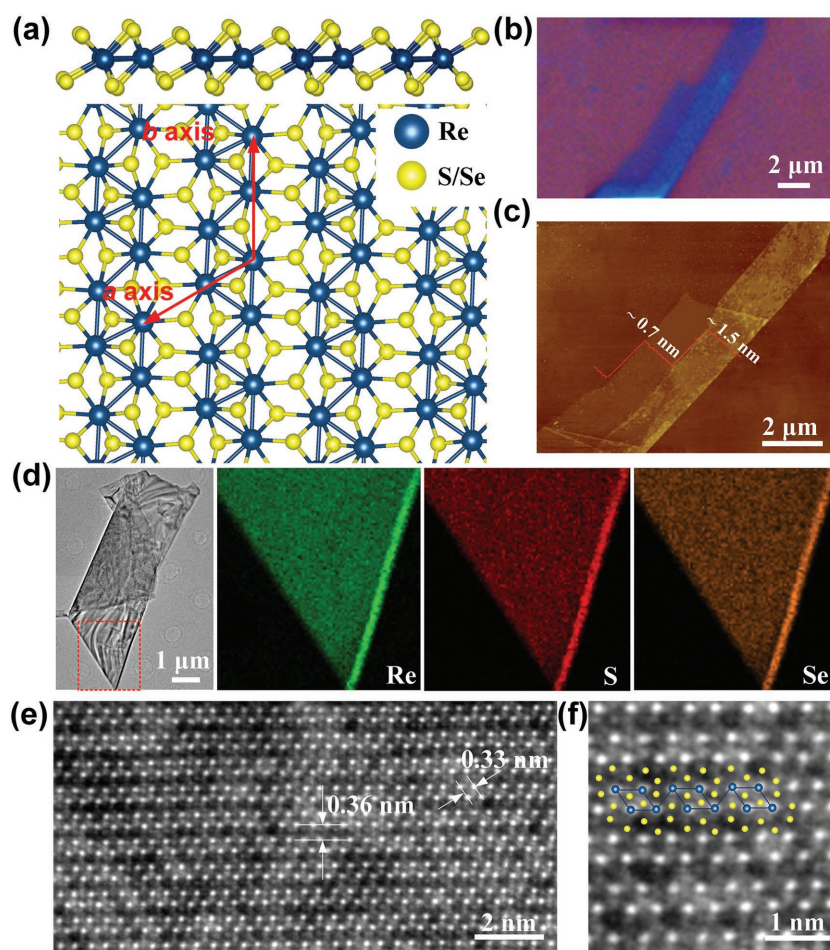National Taiwan University of Science and Technology
Taipei 106, Taiwan, Republic of China

Figure 1. a) Crystal structure of $ReS_{2(1-x)}Se_{2x}$ monolayer (side view in the top panel and top view in the bottom panel). b) Optical microscopy image and c) AFM topography of a $ReS_{1.02}Se_{0.98}$ flake on SiO_2/Si substrate. d) TEM image and EDS elemental mapping of Re, S, and Se. e) STEM image of $ReS_{1.02}Se_{0.98}$. f) Zoomed-in STEM image of $ReS_{1.02}Se_{0.98}$.

of BPs by controlling the layer number, the bandgap of ReX_2 is weakly dependent on the layer number.[10,29] Alloying, as a widely used approach to engineering the bandgap of 2D materials, can be used to tune anisotropic properties of ReX_2, such as bandgap, polarized Raman, and anisotropic charge transport behaviors.[30–33] In prior reports by Ho et al., crystals structure and band transition of bulk ReX_2 alloys have been extensively investigated.[34]

Here, we present a systematic investigation on composition-dependent photoluminescence (PL), polarized Raman spectroscopy, and anisotropic electrical transport of $ReS_{2(1-x)}Se_{2x}$ $(0 \leq x \leq 1)$ monolayer and few-layers. The PL emission energy can be continuously tuned from 1.62 eV in ReS_2 to 1.31 eV in $ReSe_2$. Combining angle-resolved polarized Raman spectroscopy and transmission electron microscopy (TEM) imaging on the same individual $ReS_{2(1-x)}Se_{2x}$ flakes, the composition-dependent Raman anisotropy has been revealed. In particular, the ReS_2-like peak at 212 and 406 cm^{-1} possesses maximum polarized Raman intensity roughly along the b and a-axis, which can be harnessed to determine the crystallographic orientation of $ReS_{2(1-x)}Se_{2x}$ alloys. Additionally, anisotropic electrical transport is maintained in $ReS_{2(1-x)}Se_{2x}$ alloys with maximum mobility along the b-axis direction and an anisotropic mobility ratio from 2.6 to 5.6.

to anisotropic electronic structure[4,8] and physical properties. So far, polarized photoluminescence emission,[9–11] polarized Raman spectroscopy,[10–12] intrinsic linear dichroism,[13,14] anisotropic in-plane thermal conductivity,[15] and anisotropic charge-carrier mobility[16] have been observed. The anisotropic physical properties permit the unique applications, such as polarization-sensitive photodetectors,[17] anisotropic field-effect transistors,[16,18] and thermoelectric devices.[15,19] However, 2D BPs suffer from chemical degradation in ambient conditions and rapid loss of device performance, which impedes their potential applications.[20,21]

As environmentally stable layered crystals, rhenium dichalcogenides (ReX_2, X = S, Se) have received considerable attention for the fabrication of functional devices with anisotropic physical properties.[22–28] The in-plane anisotropy of ReX_2 arises from the distorted 1T structure, that is, Re atoms forming zigzag chains of diamond-shaped Re4 clusters due to the Peierls transition (**Figure 1**a).[19–21] Owing to the low-symmetry lattice of ReX_2, charge-carrier mobility is higher along the crystallographic orientation parallel to the Re chains (b-axis) and lower along the direction of a-axis.[19] However, different from the widely tunable bandgap

2. Results and Discussion

Crystal structure of $ReS_{2(1-x)}Se_{2x}$ alloy is shown in Figure 1a, in which the b axis is along the direction of Re4 atomic chains. The angle between a and b axes is 119.8° for both ReS_2 and $ReSe_2$.[31] $ReS_{2(1-x)}Se_{2x}$ monolayer and few-layers were mechanically exfoliated from bulk crystals onto Si/SiO_2 substrates (300 nm oxide). A typical optical microscopy image of exfoliated $ReS_{2(1-x)}Se_{2x}$ $(x = 0.49)$ is shown in Figure 1b, which contains monolayer and bilayer regions according to the optical contrast. Atomic force microscopy (AFM) was performed in the same regions, showing a 0.7 nm height for the single layer and 1.5 nm for the bilayers. Transmission electron microscopy (TEM) and energy-dispersive X-ray spectroscopy (EDS) mapping were performed and the results revealed homogeneous spatial distribution of Re, S, and Se elements (Figure 1d). The x values of $ReS_{2(1-x)}Se_{2x}$ alloys were determined by EDS measurement (listed in Table S1, Supporting Information).

High-angle annular dark-field scanning transmission electron microscopy (HAADF-STEM) was performed on

$ReS_{1.02}Se_{0.98}$ monolayer (Figure 1e), in which diamond-shaped Re4 clusters and zigzag Re chains can be clearly seen. Due to the much smaller atomic numbers of S ($Z = 16$) and Se ($Z = 34$) than that of Re ($Z = 77$), the brightness of X_2 sites is much dimmer than that of Re sites. Then X_2 sites (S_2, SSe, or Se_2) cannot be clearly discriminated (Figure 1f). The spacing between two Re atomic chains along b and a-axes are 0.36 and 0.33 nm, respectively, which is between that of ReS_2 (0.34 and 0.31 nm) and $ReSe_2$ (0.39 and 0.35 nm).[35] Due to similar atomic radii of S (105 ± 3 pm) and Se (120 ± 4 pm), no obvious lattice distortion or deformation of Re4 chains is discovered.

PL measurement was performed on $ReS_{2(1-x)}Se_{2x}$ alloys to evaluate the alloy effect on the bandgap. $ReSe_2$ is an indirect bandgap while the bandgap type of ReS_2 is under disputation.[22,26,36] The bandgap of ReS_2 and $ReSe_2$ only change less than 0.1 eV from the bulk to monolayers owing to the interlayer coupling.[10,11,29] The PL emission of $ReS_{2(1-x)}Se_{2x}$ shows composition-dependent bandgap (**Figure 2**). In the bulk $ReS_{2(1-x)}Se_{2x}$, PL emission energy decreases from 1.52 to 1.26 eV, when the x value gradually varies from 0 to 1 (Figure 2a,b). While for the $ReS_{2(1-x)}Se_{2x}$ monolayer, its PL emission energy decreases from 1.62 to 1.31 eV (Figure 2c,d). The composition-dependent PL emission can be fitted by the following function based on the bowing effect[32]

$$E_{PL,ReS_{2(1-x)}Se_{2x}} = 2xE_{PL,ReSe_2}$$
$$-2(1-x)E_{PL,ReS_2} - 4bx(1-x) \quad (1)$$

where b is the bowing parameter. The experiment results of bulk and monolayer alloys can be fitted using Equation (1), yielding similar bowing parameters for the bulk ($b = 0.091$ eV) and the monolayer ($b = 0.099$ eV).

Raman spectroscopy provides a high-efficiency and nondestructive approach to investigate lattice vibration dynamics of $ReS_{2(1-x)}Se_{2x}$.[10–12,37] ReS_2 and $ReSe_2$ belong to the point group C_i, yielding 36 irreducible phonon modes at the Brillouin zone center, which can be written as $\Gamma = 18$ ($A_u + A_g$).[24,26] Theoretically, 18 Raman-active vibrational modes can be observed (summarized in Tables S2 and S3, Supporting Information) for both ReS_2 and $ReSe_2$ which are all A_g-like modes.[24,26] In our experiments, due to the overlapping of some Raman modes,[25] 17 and 15 Raman peaks have been observed for ReS_2 and $ReSe_2$, respectively. Typical unpolarized Raman spectra of $ReS_{2(1-x)}Se_{2x}$ monolayer with different Se compositions are shown in **Figure 3**a. For

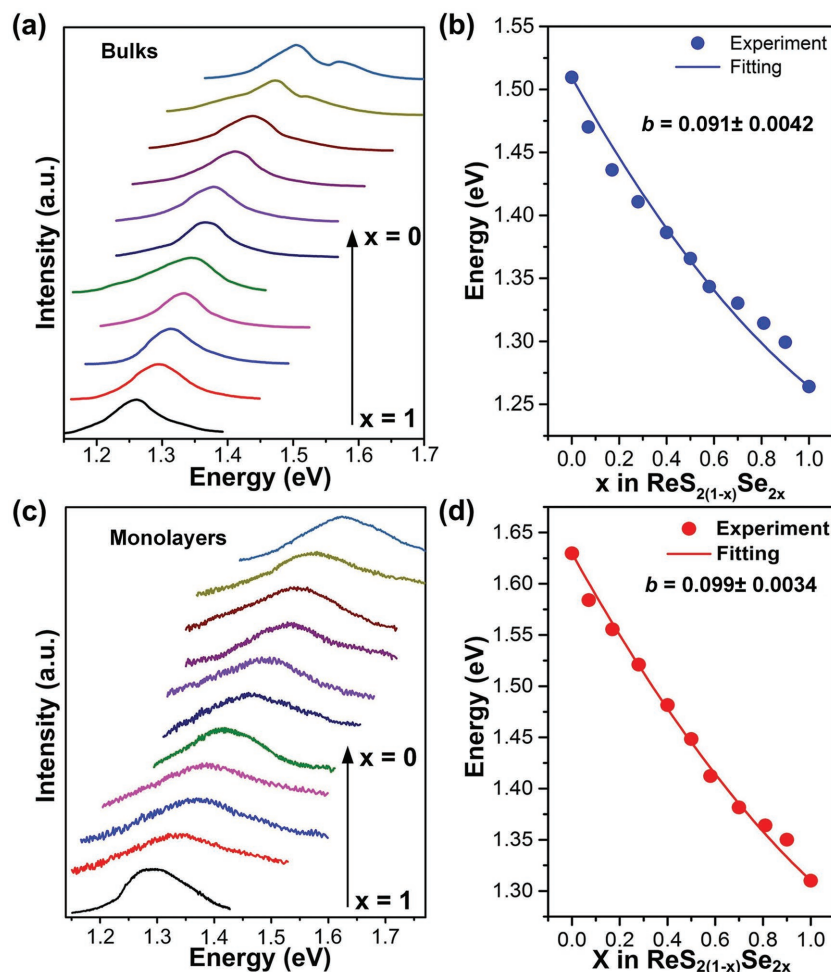**Figure 2.** a,c) Composition-dependent PL spectra and b,d) composition-dependent PL emission energy of $ReS_{2(1-x)}Se_{2x}$ bulks and monolayers, respectively.

the ReS_2 monolayer, vibration modes are in the range of 100–450 cm^{-1}, while for $ReSe_2$ monolayer, vibration modes are located below 300 cm^{-1}.

Raman frequency for all modes red shifts as Se content increases (Figure 3a–c), which results from heavier reduced mass for higher Se content in the alloys. In the lower frequency region (100–160 cm^{-1}), four sets of Raman peaks centered at 133.7, 149.6, 160.6, and 212.1 cm^{-1} have been observed for ReS_2, corresponding to the peaks at 107.6, 118.2, 124.2, and 171.7 cm^{-1} for $ReSe_2$.[38] The peak position is determined by carefully resolving the peaks (Figure S1, Supporting Information) by Lorentzian fitting. For these lower-frequency Raman modes, the peak intensity is independent of the content of S and Se in $ReS_{2(1-x)}Se_{2x}$, indicating that those modes are mainly attributed to the vibrations related to Re atoms. For the Raman shift ranging from 300 to 450 cm^{-1}, as Se content increases, the Raman peaks disappear, suggesting that these Raman peaks correspond to the vibrations related with S atoms. In middle-frequency region (from 160 to 300 cm^{-1}), abundant peaks were observed for $ReSe_2$ and $ReS_{2(1-x)}Se_{2x}$ with high Se content, while only few peaks were observed for ReS_2 and $ReS_{2(1-x)}Se_{2x}$ with low Se content (Figure S2, Supporting Information). Additionally, most Raman modes
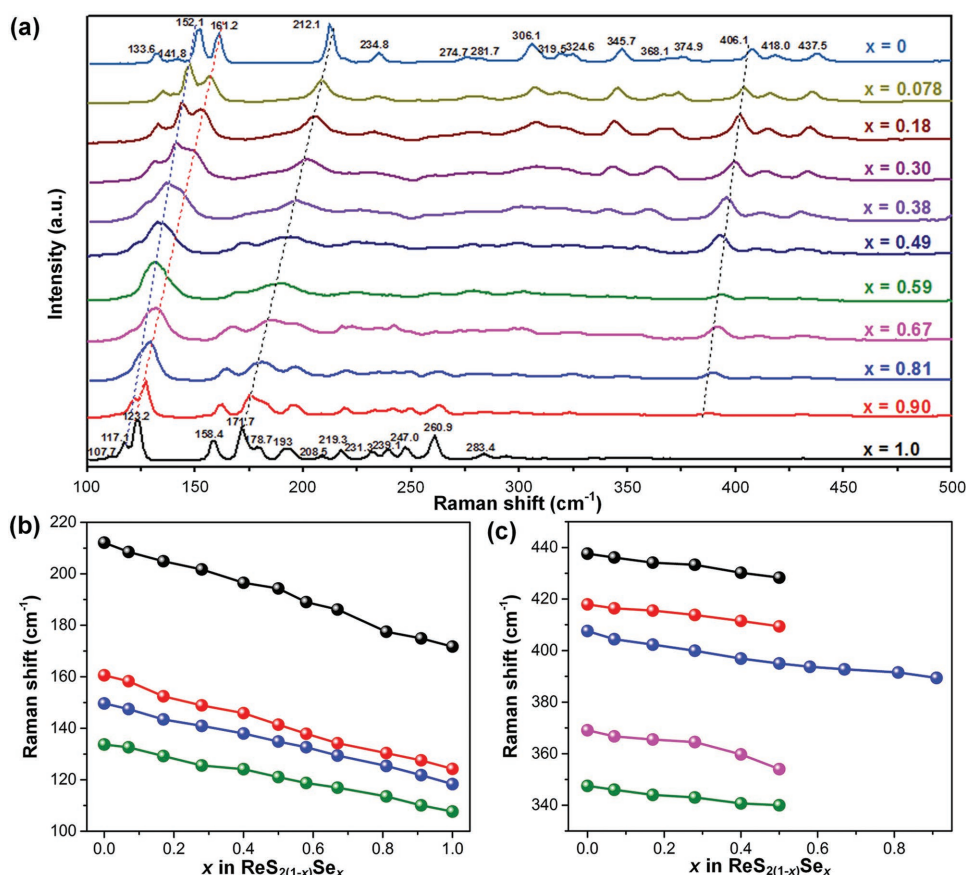
Figure 3. a) Composition-dependent Raman spectra of $ReS_{2(1-x)}Se_{2x}$ monolayers. Evolution of Raman peak positions of $ReS_{2(1-x)}Se_{2x}$ in the range of b) 100–220 and c) 290–500 cm^{-1}.

in $ReS_{2(1-x)}Se_{2x}$ alloys show layer-independent frequency (Figures S3 and S4, Supporting Information), similar to that observed in ReS_2 and $ReSe_2$.[11,29]

To gain further insights into the lattice anisotropy of $ReS_{2(1-x)}Se_{2x}$ alloys, we performed angle-resolved polarized Raman characterization. *XX*-configuration (i.e., parallel excitation and scattering) polarized Raman measurement at different laser-polarization-to-*b*-axis rotation angles was employed. Polarized Raman spectra were collected by rotating the sample with a step of 10° (accuracy of ≈±2°). After the polarized Raman characterization, the same sample was transferred onto TEM grid for determining the crystallographic orientation. **Figure 4** presents a typical TEM and polarized Raman measurement on the same $ReS_{1.02}Se_{0.98}$ flake. Figure 4a shows a representative $ReS_{1.02}Se_{0.98}$ few-layer with straight edges. High-resolution TEM image (Figure 4b) of this sample illustrates a set of lattice plane with an interplane distance of 0.34 nm, which can be assigned to the interchain distance of Re atomic chains. Through comparing low-magnification (Figure S5, Supporting Information) and high-resolution TEM results, the long cleavage edge can be determined to be *b*-axis direction. The *b*-axis direction was always defined as the 0° polarization angle in all polarized Raman measurements.

Polarized Raman intensity of $ReS_{1.02}Se_{0.98}$ few-layers was mapped in Figure 4c,d, illustrating strong angle-dependence and Raman-mode dependence. Raman peaks at around

141, 194, and 428 cm^{-1} show maximum intensities along or approximately along *b*-axis. Raman peaks at around 134, 231, 301, 315, 359, and 409 cm^{-1} show maximum intensities along directions between *a*- and *b*-axes. For each Raman mode, different values of matrix elements in the Raman tensors can induce the different anisotropic Raman behaviors. Here, we focused on two Raman modes with peaks centering at 194 and 395 cm^{-1} in $ReS_{1.02}Se_{0.98}$, which has a maximum intensity around the direction of *b*- and *a*-axes. These two peaks are corresponding to 212 and 406 cm^{-1} peaks in ReS_2. For ReX_2 crystals (C_i symmetry), all Raman active modes have a Raman tensor R in the same form of[10]

$$R = \begin{bmatrix} a & d & e \\ d & b & f \\ e & f & c \end{bmatrix} \tag{2}$$

The Raman mode intensity can be expressed as a function of the crystal symmetry and polarization geometry as below[12]

$$I \propto |e_s R e_i|^2 \tag{3}$$

where e_i and e_s are unit polarization vector of the electric field of the incident and scattered light, respectively. In our case, the incident and scattered light is parallel polarized
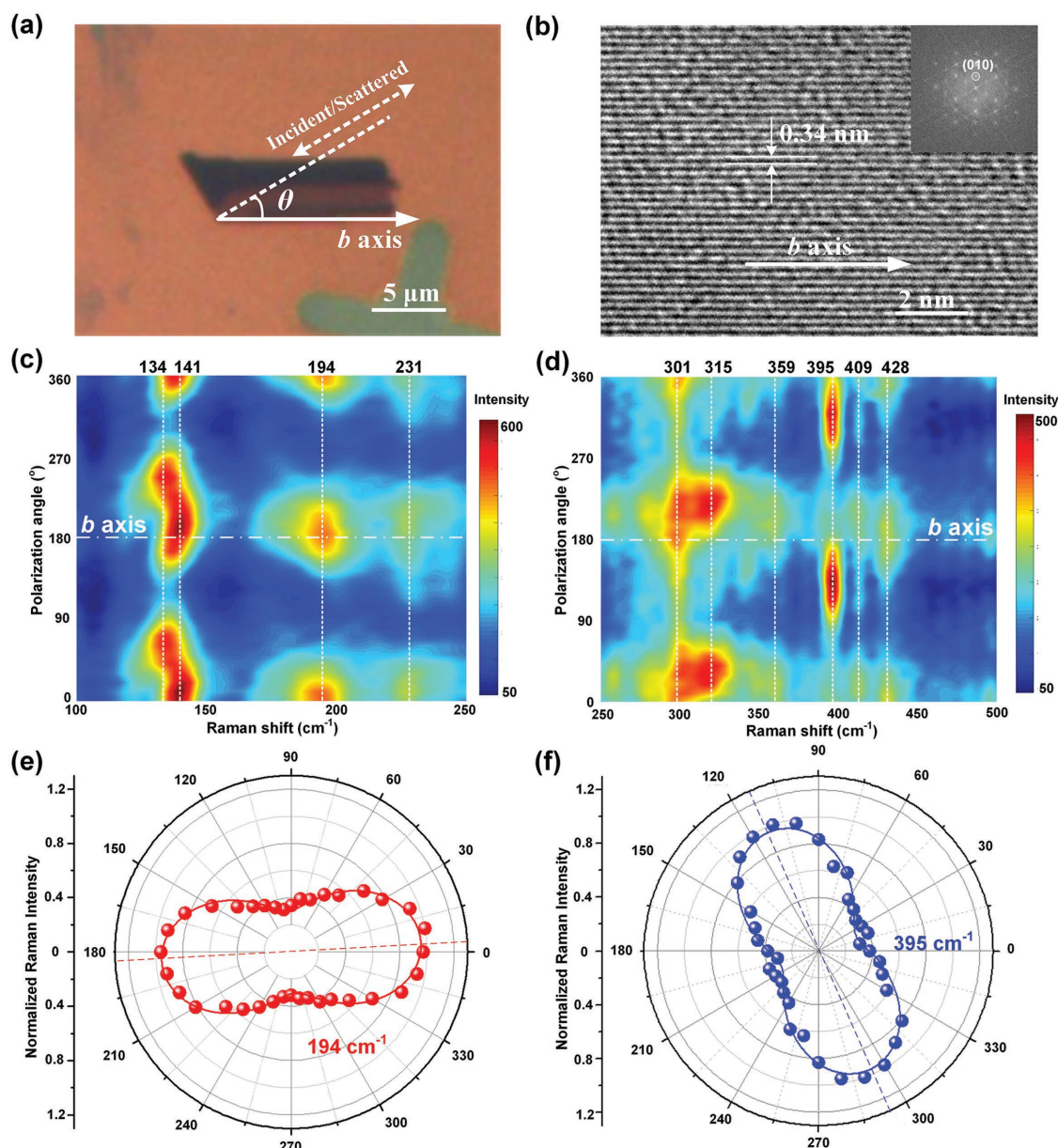
Figure 4. a) Optical microscopy image, b) TEM image, c,d) false-color plot of polarized Raman intensity, and polar plot and fitting of e) 194 and f) 395 cm^{-1} peak of the same ReS$_{1.02}$Se$_{0.98}$ few-layers.

(i.e., *XX*-configuration) and the angle between polarization vector and relative to the *b*-axis is defined as θ. Then e_i and e_s can be given with the following format

$$e_s = \begin{bmatrix} \cos\theta & \sin\theta & 0 \end{bmatrix}, e_i = \begin{bmatrix} \cos\theta \\ \sin\theta \\ 0 \end{bmatrix} \qquad (4)$$

By combining Equation (2) to (4), the polarized Raman intensity at *XX*-configuration can be written as

$$I \propto \left| a\cos^2\theta + b\sin^2\theta + d\sin 2\theta \right|^2 \qquad (5)$$

The experimental data can be well fitted by Equation (5). The maximum intensity of 194 cm^{-1} peak

is at around 4°, that is, close to the direction of *b*-axis (Figure 4e). Polarized Raman measurements and TEM characterizations for the same ReS$_{2(1−x)}$Se$_{2x}$ few-layer with other Se contents are shown in Figures S6–S12 (Supporting Information).

As Se composition changes, the polarization direction of ReS$_2$-like peak at 212 cm^{-1} branch (red data points in **Figure 5**a–f) gradually deviates from the *b*-axis direction with increasing Se content. In ReSe$_2$, the maximum Raman intensity direction reaches ≈17° away from the *b*-axis. According to the previous report,[24] the ReS$_2$-like peak at 212 cm^{-1} is mainly contributed by the in-plane vibration of Re atoms along the *b*-axis. With the substitution of S with Se atoms, vibration of Re atoms is more susceptible to surrounding Se atoms with larger atomic mass. For the other peak (ReS$_2$-like peak at 406 cm^{-1}, blue data points in Figure 5a–f), the
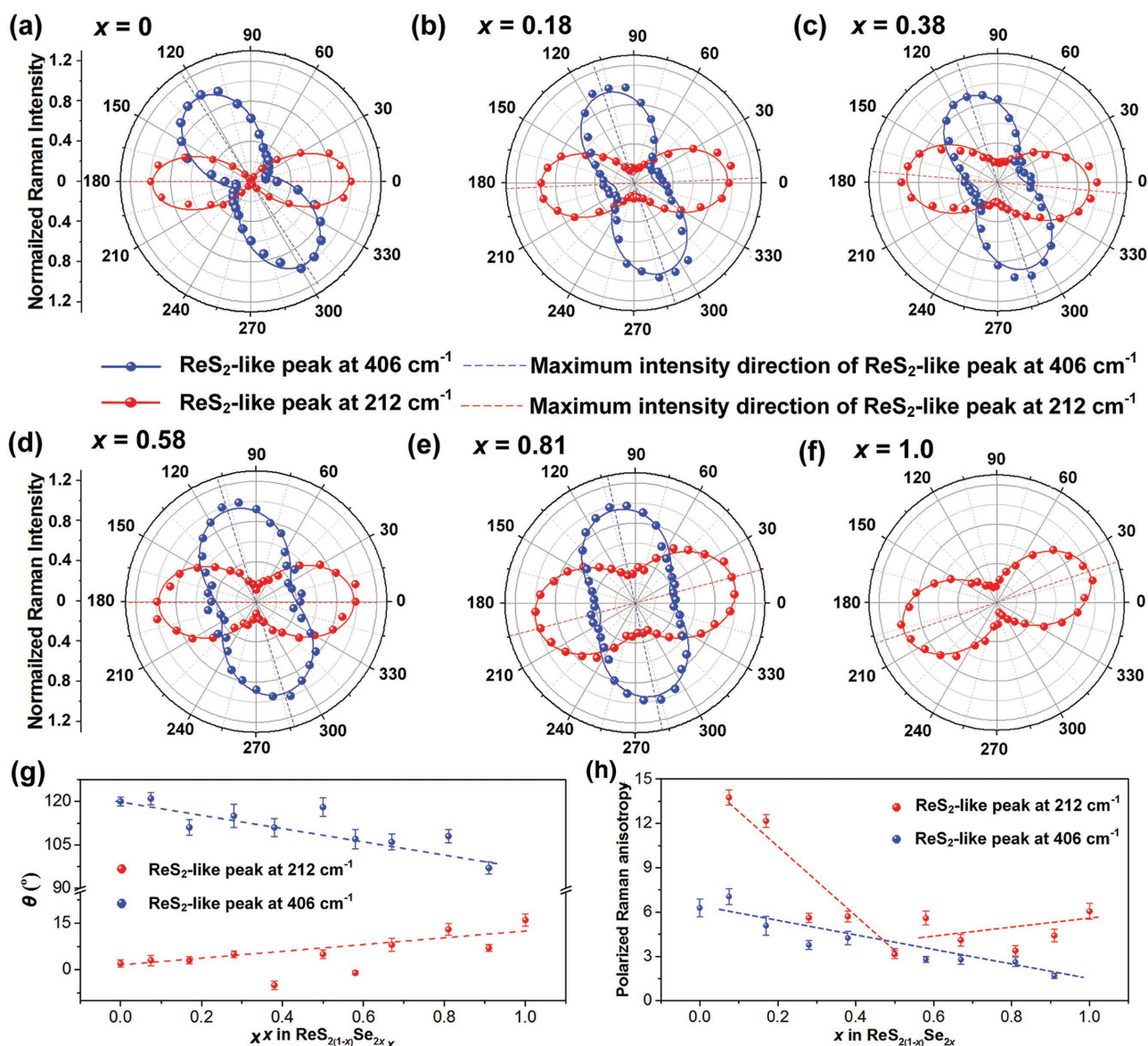
Figure 5. Angle-dependent Raman intensity of ReS$_2$-212 cm^{-1} (red dots) and ReS$_2$-406 cm^{-1} (blue dots) branches in ReS$_{2(1-x)}$Se$_{2x}$: a) ReS$_2$, b) ReS$_{1.64}$Se$_{0.36}$, c) ReS$_{1.24}$Se$_{0.76}$, d) ReS$_{0.84}$Se$_{1.16}$, e) ReS$_{0.38}$Se$_{1.62}$, and f) ReSe$_2$. The *b*-axis is at 0° in (a–f). Plot of g) polarization angle and h) intensity anisotropic ratio for the ReS$_2$ 212 and 406 cm^{-1} branches in ReS$_{2(1-x)}$Se$_{2x}$.

maximum Raman intensity direction (along the *a*-axis) is maintained.

Another observation is that the anisotropic ratio of Raman intensity (I_{max}/I_{min}) changes with Se content (Figure 5g,h). For ReS$_2$-like peak at 212 cm^{-1}, it is clearly seen that I_{max}/I_{min} is larger in the two end materials (ReS$_2$ and ReSe$_2$) while I_{max}/I_{min} is smaller in ReS$_{2(1-x)}$Se$_{2x}$ alloys. This could be due to alloying-induced disorder which can degrade the anisotropic ratio. For ReS$_2$-like peak at 406 cm^{-1}, since it relates with S vibration, I_{max}/I_{min} decreases as Se content increases and the peak is absent in ReSe$_2$.

To investigate the electrical transport properties of 2D ReS$_{2(1-x)}$Se$_{2x}$, field-effect transistors (FETs) were fabricated. Typical transfer curves of 2D ReS$_{2(1-x)}$Se$_{2x}$ (thickness in the range of 1–5 layers) at different drain–source voltages are shown in **Figure 6**a–c (FET channel length around 1 μm). N-type transport with high on-off ratio of 10^5–10^7 has been

observed. Charge-carrier mobility can be extracted from transfer curves by

$$\mu_{FE} = \frac{dI_{ds}}{dV_{gs}} \frac{L}{W} \frac{1}{C_i V_{ds}} \tag{6}$$

where L and W are channel length and width of FETs, C_i is the capacitance of gate dielectric layer, I_{ds} is the drain–source current, and V_{ds} and V_{gs} are the drain–source and gate voltages, respectively. The electrodes were randomly patterned on ReS$_{2(1-x)}$Se$_{2x}$. At least four FETs were measured for each composition. Higher mobilities are observed in end member ReS$_2$ and ReSe$_2$, while ReS$_{2(1-x)}$Se$_{2x}$ ($0.1 \leq x \leq 0.9$) alloys exhibit lower charge transport performance (Figure 6d). The relatively low charge transport performances of alloys may be due to the disorder-induced carrier scattering. The conductivity (at V_{gs} of 40 V) of 2D ReS$_{2(1-x)}$Se$_{2x}$ shows similar
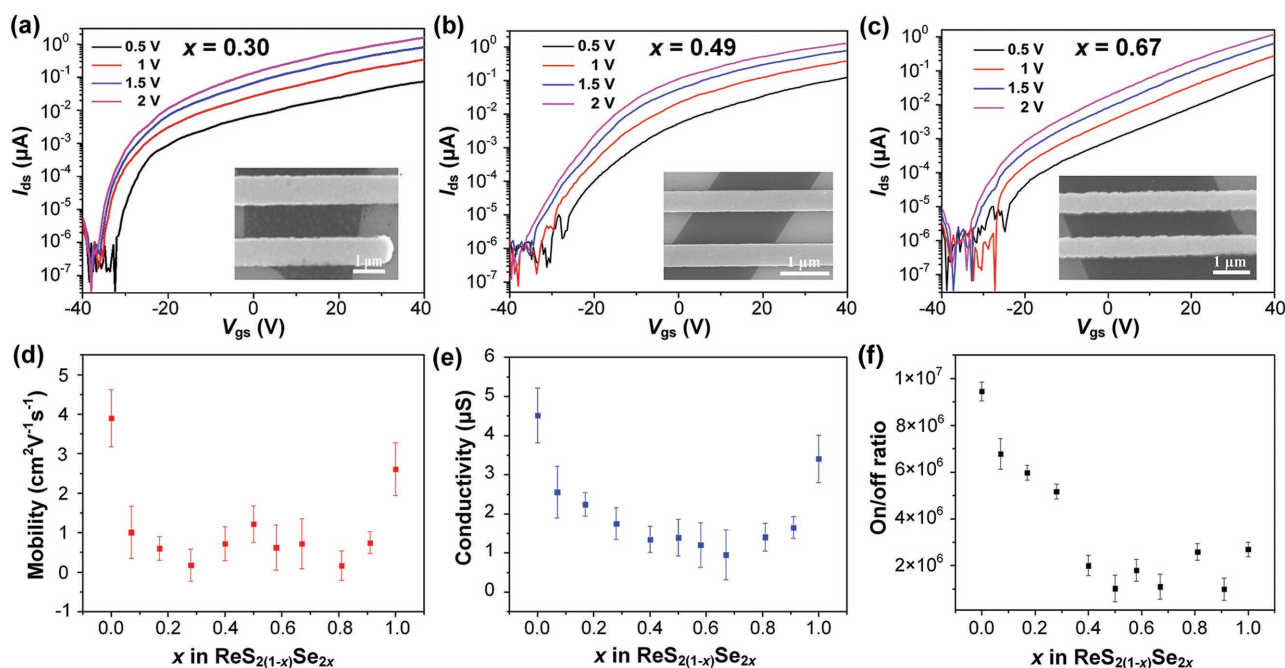
Figure 6. Transfer curves of a) $ReS_{1.40}Se_{0.60}$, b) $ReS_{1.02}Se_{0.98}$, and c) $ReS_{0.66}Se_{1.34}$. Composition-dependent d) mobility, e) conductivity, and f) on/off ratio of $ReS_{2(1-x)}Se_{2x}$.

composition-dependence as carrier mobility (Figure 6e). On/off ratio decreases slightly with the substitution of S by Se atoms (Figure 6f), which may be due to lower bandgap of $ReS_{2(1-x)}Se_{2x}$ with higher Se content.

Furthermore, angle-resolved transport characterization was carried out to measure anisotropic electrical properties of $ReS_{2(1-x)}Se_{2x}$ few-layers. In experiments, 12 electrodes were fabricated on individual $ReS_{2(1-x)}Se_{2x}$ few-layers spaced at an angle of 30°. After measurements of anisotropic electrical transport, we performed Raman and transferred the $ReS_{2(1-x)}Se_{2x}$ to the TEM grid to determine the crystallographic orientation. The directions of b-axis were determined by TEM and defined as 0° for polarized Raman spectra and electron mobility. Representative optical microscopy image displays the homogeneous channel width and length of devices (**Figure 7**a–c, inset). The TEM images of the 2D alloys with electrodes illustrate the morphology of $ReS_{2(1-x)}Se_{2x}$ in the electronic measurements (Figure S13, Supporting Information). The corresponding high-resolution TEM images illustrate the direction of b-axis (Figure 7a–c, inset), which are parallel to the long cleaved side of $ReS_{2(1-x)}Se_{2x}$ sheets. At all different angles, $ReSe_2$, $ReS_{0.38}Se_{1.62}$, and $ReS_{1.02}Se_{0.98}$ few-layers show n-type transport with on-current larger than 1 µA and off-current ≈1 pA (on/off ratio ≈10^6). The on current shows anisotropic behavior (Figure 7a–c). The mobility is in the range of 2.12–6.16, 1.44–5.53, and 1.26–8.45 cm² V⁻¹ s⁻¹ for $ReSe_2$, $ReS_{0.38}Se_{1.62}$, and $ReS_{1.02}Se_{0.98}$ few-layers, respectively, with a maximum mobility along b-axis (Figure 7d–f). Other $ReS_{2(1-x)}Se_{2x}$ few-layers also show similar anisotropic electrical transport (Figures S14 and S15, Supporting Information). The anisotropic mobility ratios for $ReS_{2(1-x)}Se_{2x}$ few-layers are also calculated to be 3.0, 5.6, 3.8, 2.6, and 2.9 for ReS_2, $ReS_{1.02}Se_{0.98}$, $ReS_{0.38}Se_{1.62}$, $ReS_{1.64}Se_{0.36}$, and $ReSe_2$, respectively. The polarization-dependent Raman intensities

of ReS_2-like peak at 212 cm⁻¹ were determined after electric measurements, which exhibit an anisotropic feature with maximum intensity roughly along the b-axis. The deviations are induced by the substitution of S with Se atoms, which are kept within 15°.

3. Conclusion

In conclusion, we have systematically investigated optical bandgap, lattice dynamics, and electrical transport characteristics of 2D $ReS_{2(1-x)}Se_{2x}$ alloys. Tunable bandgap in the range of 1.31–1.62 eV has been obtained in anisotropic $ReS_{2(1-x)}Se_{2x}$ monolayers. Anisotropic Raman scattering has been observed for all bands in $ReS_{2(1-x)}Se_{2x}$. Few-layer $ReS_{2(1-x)}Se_{2x}$ also show anisotropic electrical transport over all compositions with anisotropic mobility along b-axis. Our research provides a fundamental understanding on lattice vibration, anisotropic electronic properties of $ReS_{2(1-x)}Se_{2x}$, which benefits electronic and optoelectronic applications based on anisotropic 2D materials.

4. Experimental Section

Fabrication of the $ReS_{2(1-x)}Se_{2x}$ Alloys: Single-crystal $ReS_{2(1-x)}Se_{2x}$ alloys were grown by chemical-vapor transport method by reaction at 1030 °C for 10 d in evacuated quartz ampoules.[34] Br_2 was used as transport agent in a quartz tube to carry the materials. The stoichiometric mixture of elements (Re, S, Se) was added into a quartz ampoule and evacuated to a pressure of 10^{-6} Torr and sealed. $ReS_{2(1-x)}Se_{2x}$ monolayers and few-layers were prepared by mechanical exfoliation of the corresponding bulk single crystals.
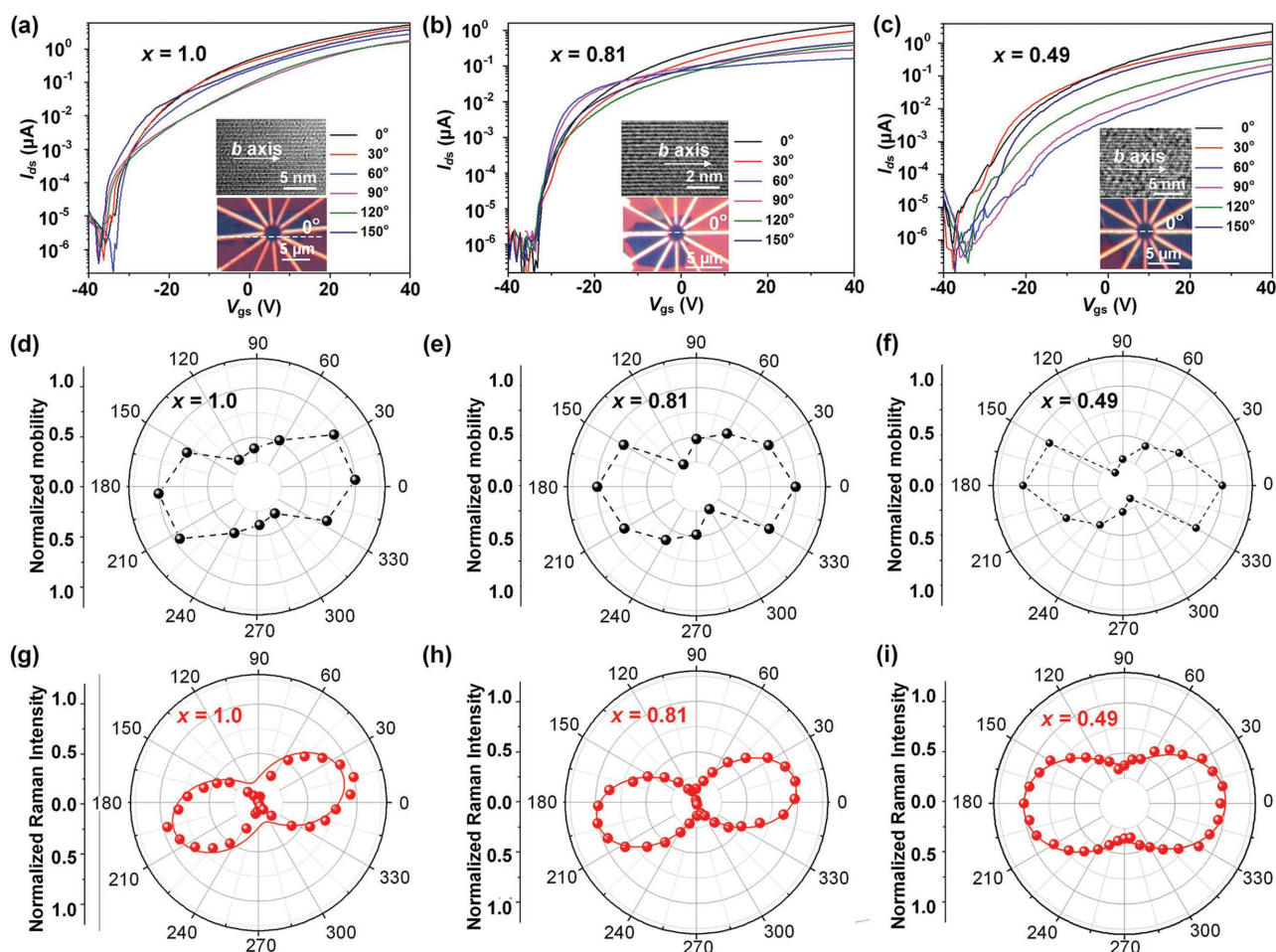
Figure 7. Anisotropic electric transport of $ReS_{2(1-x)}Se_{2x}$ alloys. a–c) Transfer curves, d–f) angle-dependent mobility, and g–i) polarized Raman intensity of ReS_2-212 cm^{-1} branch. a,d,g) $ReSe_2$, b,e,h) $ReS_{0.38}Se_{1.62}$, and c,f,i) $ReS_{1.02}Se_{0.98}$. Inset in (a–c) optical microscopy image and HRTEM image of $ReS_{2(1-x)}Se_{2x}$.

Characterizations: SEM imaging was carried out on a Hitachi S-4800 operating at 2.0 kV. TEM imaging and EDS characterization were done on FEI Tecnai G2 F20 U-TEIN operated at 200 kV. TEM samples were prepared by transferring the $ReS_{2(1-x)}Se_{2x}$ flakes onto small lacey formvar/carbon film TEM grids (BZ110120A) by a poly(methyl methacrylate) (PMMA)-mediated nanotransfer method.[39] AFM imaging was done on a Veeco Dimension 3100 with tapping mode. STEM characterization was carried out on a probe-corrected Titan Chemi STEM at an acceleration voltage of 200 kV. Raman spectroscopy was done on a micro-Raman spectrometer (Renishaw in Via plus at 514.5 nm laser), a 100× objective (NA = 0.9, corresponding *XY* resolution of ≈1 μm), and an 1800 lines mm^{-1} grating. Photoluminescence was measured with a Horiba HR800 Raman system with a liquid-nitrogen-cooled InGaAs detector. Polarized Raman spectra were acquired by adding two parallel polarizer in the incident and scattering optical paths, respectively, and rotating the sample with 10° intervals.

Device Fabrication and Electrical Measurement: Electron beam lithography and thermal evaporation were used for device fabrication. Ti/Au (5 nm and 50 nm) was used as contact electrodes. The electrical measurements were performed on an Agilent B1500A semiconductor device analyzer in a vacuum (Janis ST500 probe station, ≈10^{-5} Torr).

Supporting Information

Supporting Information is available from the Wiley Online Library or from the author.

Acknowledgements

![small NANO MICRO logo]

[1] G. Fiori, F. Bonaccorso, G. Iannaccone, T. Palacios, D. Neumaier, A. Seabaugh, S. K. Banerjee, L. Colombo, *Nat. Nanotechnol.* **2014**, *9*, 768.

[2] Q. H. Wang, K. Kalantar-Zadeh, A. Kis, J. N. Coleman, M. S. Strano, *Nat. Nanotechnol.* **2012**, *7*, 699.

[3] L. Britnell, R. M. Ribeiro, A. Eckmann, R. Jalil, B. D. Belle, A. Mishchenko, Y.-J. Kim, R. V. Gorbachev, T. Georgiou, S. V. Morozov, A. N. Grigorenko, A. K. Geim, C. Casiraghi, A. H. C. Neto, K. S. Novoselov, *Science* **2013**, *340*, 1311.

[4] X. Wang, A. M. Jones, K. L. Seyler, V. Tran, Y. Jia, H. Zhao, H. Wang, L. Yang, X. Xu, F. Xia, *Nat. Nanotechnol.* **2015**, *10*, 517.

[5] B. Radisavljevic, A. Radenovic, J. Brivio, V. Giacometti, A. Kis, *Nat. Nanotechnol.* **2011**, *3*, 147.

[6] V. Tran, R. Soklaski, Y. Liang, L. Yang, *Phys. Rev. B* **2014**, *89*, 235319.

[7] R. J. Wu, M. Topsakal, T. Low, M. C. Robbins, N. Haratipour, J. S. Jeong, R. M. Wentzcovitch, S. J. Koester, K. A. Mkhoyan, *J. Vac. Sci. Technol., A* **2015**, *33*, 060604.

[8] D. Çakır, C. Sevik, F. M. Peeters, *Phys. Rev. B* **2015**, *92*, 165406.

[9] R. Xu, S. Zhang, F. Wang, J. Yang, Z. Wang, J. Pei, Y. W. Myint, B. Xing, Z. Yu, L. Fu, Q. Qin, Y. Lu, *ACS Nano* **2016**, *10*, 2046.

[10] H. Zhao, J. Wu, H. Zhong, Q. Guo, X. Wang, F. Xia, L. Yang, P. Tan, H. Wang, *Nano Res.* **2015**, *8*, 3651.

[11] X. F. Qiao, J. B. Wu, L. W. Zhou, J. Qiao, W. Shi, T. Chen, X. Zhang, J. Zhang, W. Ji, P. H. Tan, *Nanoscale* **2016**, *9*, 8324.

[12] X. Zhang, Q. H. Tan, J. B. Wu, W. Shi, P. H. Tan, *Nanoscale* **2016**, *8*, 6435.

[13] J. Qiao, X. Kong, Z.-X. Hu, F. Yang, W. Ji, *Nat. Commun.* **2014**, *5*, 5475.

[14] X. Ling, S. Huang, E. H. Hasdeo, L. Liang, W. M. Parkin, Y. Tatsumi, A. R. T. Nugraha, A. A. Puretzky, P. M. Das, B. G. Sumpter, D. B. Geohegan, J. Kong, R. Saito, M. Drndic, V. Meunier, M. S. Dresselhaus, *Nano Lett.* **2016**, *4*, 2260.

[15] S. Lee, F. Yang, J. Suh, S. Yang, Y. Lee, G. Li, H. Sung Choe, A. Suslu, Y. Chen, C. Ko, J. Park, K. Liu, J. Li, K. Hippalgaonkar, J. J. Urban, S. Tongay, J. Wu, *Nat. Commun.* **2015**, *6*, 8573.

[16] F. Xia, H. Wang, Y. Jia, *Nat. Commun.* **2014**, *5*, 4458.

[17] H. Yuan, X. Liu, F. Afshinmanesh, W. Li, G. Xu, J. Sun, B. Lian, A. G. Curto, G. Ye, Y. Hikita, Z. Shen, S.-C. Zhang, X. Chen, M. Brongersma, H. Y. Hwang, Y. Cui, *Nat. Nanotechnol.* **2015**, *10*, 707.

[18] L. Li, Y. Yu, G. J. Ye, Q. Ge, X. Ou, H. Wu, D. Feng, X. H. Chen, Y. Zhang, *Nat. Nanotechnol.* **2014**, *9*, 372.

[19] Y. Wang, G. Xu, Z. Hou, B. Yang, X. Zhang, E. Liu, X. Xi, Z. Liu, Z. Zeng, W. Wang, G. Wu, *Appl. Phys. Lett.* **2016**, *108*, 092102.

[20] A. Favron, E. Gaufres, F. Fossard, A.-L. Phaneuf-Lheureux, Y. W. Tang, P. L. Levesque, A. Loiseau, R. Leonelli, S. Francoeur, R. Martel, *Nat. Mater.* **2015**, *14*, 826.

[21] J. D. Wood, S. A. Wells, D. Jariwala, K.-S. Chen, E. Cho, V. K. Sangwan, X. Liu, L. J. Lauhon, T. J. Marks, M. C. Hersam, *Nano Lett.* **2014**, *14*, 6964.

[22] E. Liu, Y. Fu, Y. Wang, Y. Feng, H. Liu, X. Wan, W. Zhou, B. Wang, L. Shao, C.-H. Ho, Y.-S. Huang, Z. Cao, L. Wang, A. Li, J. Zeng, F. Song, X. Wang, Y. Shi, H. Yuan, H. Y. Hwang, Y. Cui, F. Miao, D. Xing, *Nat. Commun.* **2015**, *6*, 6991.

[23] H.-X. Zhong, S. Gao, J.-J. Shi, L. Yang, *Phys. Rev. B* **2015**, *92*, 115438.

[24] Y. Feng, W. Zhou, Y. Wang, J. Zhou, E. Liu, Y. Fu, Z. Ni, X. Wu, H. Yuan, F. Miao, B. Wang, X. Wan, D. Xing, *Phys. Rev. B* **2015**, *92*, 054110.

[25] D. A. Chenet, O. B. Aslan, P. Y. Huang, C. Fan, A. M. van der Zande, T. F. Heinz, J. C. Hone, *Nano Lett.* **2015**, *15*, 5667.

[26] D. Wolverson, S. Crampin, A. S. Kazemi, A. Ilie, S. J. Bending, *ACS Nano* **2014**, *8*, 11154.

[27] E. Zhang, Y. Jin, X. Yuan, W. Wang, C. Zhang, L. Tang, S. Liu, P. Zhou, W. Hu, F. Xiu, *Adv. Funct. Mater.* **2015**, *25*, 4076.

[28] F. Liu, S. Zheng, X. He, A. Chaturvedi, J. He, W. L. Chow, T. R. Mion, X. Wang, J. Zhou, Q. Fu, H. J. Fan, B. K. Tay, L. Song, R.-H. He, C. Kloc, P. M. Ajayan, Z. Liu, *Adv. Funct. Mater.* **2016**, *26*, 1169.

[29] S. Tongay, H. Sahin, C. Ko, A. Luce, W. Fan, K. Liu, J. Zhou, Y.-S. Huang, C.-H. Ho, J. Yan, D. F. Aloni, S. Ogletree, J. Ji, S. Li, J. Li, F. M. Peeters, J. Wu, *Nat. Commun.* **2014**, *5*, 3252.

[30] H. Li, X. Duan, X. Wu, X. Zhuang, H. Zhou, Q. Zhang, X. Zhu, W. Hu, P. Ren, P. Guo, L. Ma, X. Fan, X. Wang, J. Xu, A. Pan, X. Duan, *J. Am. Chem. Soc.* **2014**, *136*, 3756.

[31] X. Duan, C. Wang, Z. Fan, G. Hao, L. Kou, U. Halim, H. Li, X. Wu, Y. Wang, J. Jiang, A. Pan, Y. Huang, R. Yu, X. Duan, *Nano Lett.* **2016**, *16*, 264.

[32] Y. Chen, J. Xi, D. O. Dumcenco, Z. Liu, K. Suenaga, D. Wang, Z. Shuai, Y.-S. Huang, L. Xie, *ACS Nano* **2013**, *7*, 4610.

[33] M. Zhang, J. Wu, Y. Zhu, D. O. Dumcenco, J. Hong, N. Mao, S. Deng, Y. Chen, Y. Yang, C. Jin, S. H. Chaki, Y.-S. Huang, J. Zhang, L. Xie, *ACS Nano* **2014**, *8*, 7130.

[34] C. H. Ho, Y. S. Huang, P. C. Liao, K. K. Tiong, *J. Phys. Chem. Sol.* **1999**, *60*, 1797.

[35] Y.-C. Lin, H.-P. Komsa, C.-H. Yeh, T. Björkman, Z.-Y. Liang, C.-H. Ho, Y.-S. Huang, P.-W. Chiu, A. V. Krasheninnikov, K. Suenaga, *ACS Nano* **2015**, *9*, 11249.

[36] G.-L. Ignacio, R. B. Aditya, U. Nicolas, F. M. Alberto, *2D Mater.* **2016**, *3*, 045016.

[37] X. Zhang, X. F. Qiao, W. Shi, J. B. Wu, D. S. Jiang, P. H. Tan, *Chem. Soc. Rev.* **2015**, *44*, 2757.

[38] D. Wolverson, L. S. Hart, *Nanoscale Res. Lett.* **2016**, *11*, 250.

[39] L. Jiao, B. Fan, X. Xian, Z. Wu, J. Zhang, Z. Liu, *J. Am. Chem. Soc.* **2008**, *130*, 12612.